

Multidisciplinary Applications of Detached-Eddy Simulation to Separated Flows at High Reynolds Numbers (Challenge 92)

Scott A. Morton*, Matthew B. Steenman†, Russell M. Cummings‡
Dept. of Aeronautics, USAF Academy

James R. Forsythe§, Kenneth E. Wurtzler¶
Cobalt Solutions, LLC

Shawn H. Woodson ||
Naval Air Systems Command

Kyle D. Squires **
*Dept. of Mechanical and Aerospace Engineering
Arizona State University*

Philippe R. Spalart ††
Boeing Commercial Airplanes

Abstract

This work focuses on multidisciplinary applications of Detached-Eddy Simulation (DES), principally flight mechanics and aeroelasticity. Specifically, the lateral instability (known as abrupt wing stall) of the pre-production F/A-18E is reproduced using DES, including the unsteady shock motion. The presence of low frequency pressure oscillations due to shock motion in the current simulations and the experiments motivated a full aircraft calculation, which showed low frequency high-magnitude rolling moments that could be a significant contributor to the abrupt wing stall phenomenon. DES is also applied to the F-18 high angle of attack research vehicle (HARV) at a moderate angle of attack to reproduce the vortex breakdown leading to vertical stabilizer buffet. Unsteady tail loads are compared to flight test data. This work lays the foundation for future deforming grid calculations to reproduce the aero-elastic tail buffet seen in flight test. Solution based grid adaption is used on unstructured grids in both cases to improve the resolution in the separated region.

Previous DoD Challenge work has demonstrated the unique ability of the DES turbulence treatment to ac-

curately and efficiently predict flows with massive separation at flight Reynolds numbers. DES Calculations have been performed using the *Cobalt* code and on unstructured grids, an approach that can deal with complete configurations with very few compromises. A broad range of flows has been examined in previous Challenge work, including aircraft forebodies, airfoil sections, a missile afterbody, vortex breakdown on a delta wing, and the F-16 and F-15E at high angles-of-attack. All DES predictions exhibited a moderate to significant improvement over results obtained using traditional Reynolds-averaged models and often excellent agreement with experimental/flight-test data. DES combines the efficiency of a Reynolds-averaged turbulence model near the wall with the fidelity of Large-Eddy Simulation (LES) in separated regions. Since it uses Large Eddy Simulation in the separated regions, it is capable of predicting the unsteady motions associated with separated flows.

The development and demonstration of improved methods for the prediction of flight mechanics and aeroelasticity in this Challenge is expected to reduce the acquisition cost of future military Aircraft.

1 Introduction

Numerical simulations are an important tool for predicting aircraft performance, especially in off-design regimes that are difficult to investigate using wind-tunnel or flight testing. While CFD for aerodynamic applications is coming of age at various labs and in universities, e.g., full-

* Associate Professor

† Cadet First Class

‡ Distinguished Visiting Professor

§ Director of Research

¶ Director of Marketing

|| Aerospace Engineer

** Professor

†† Technical Fellow

airplane computations are now possible, one of the main stumbling blocks to the increased use of CFD for design and analysis has been an inability to accurately predict the unsteady effects of massive flow separations. Recent efforts on predicting massively separated flows around full aircraft at flight Reynolds numbers, however, has shown that Detached-Eddy Simulation (DES) is a viable method for use in this difficult flow regime. The present investigators have predicted the massively separated flow over several aircraft with DES predictions in good agreement with experiments or flight-test data (Forsythe *et al.* [1], Squires *et al.* [2]). These successful efforts motivate the present research - extension of DES to multidisciplinary applications. The two applications considered are flight mechanics and aeroelasticity. The algorithm requirements in extending the current simulation methodology into these areas are similar – principally the use of grid speed terms. The present work focuses on laying the foundation for subsequent grid motion (both deforming and rigid body) calculations. The cases considered are the abrupt wing stall (AWS) of the pre-production F/A-18E and vortex breakdown of the F-18C. This represents both flight mechanics (lateral instability) and aeroelasticity (tail buffet) of full aircraft.

2 Problem and Methodology

2.1 Abrupt Wing Stall

During envelope expansion flights of the F/A-18E/F in the Engineering and Manufacturing Development phase, the aircraft encountered uncommanded lateral activity, which was labeled “wing drop”. An extensive resolution process was undertaken by the Navy and its contractors to resolve this issue. A production solution was developed, which included revising the flight control laws and the incorporation of a porous wing fold fairing to eliminate the wing drop tendencies of the pre-production F/A-18E/F. The wing drop events were traced to an abrupt wing stall (AWS) on either the left or right wing panel, causing a sudden and severe roll-off in the direction of the stalled wing. An important distinction between wing drop and AWS is that wing drop is the dynamic response of an aircraft to an aerodynamic event, while AWS is an aerodynamic event that can trigger a wing drop.[3]

Unsteady measurements on a model of a pre-production F/A-18E were made by Schuster and Byrd [4], motivated by the following statement: “Since AWS and the resulting lateral instabilities are dynamic or, at best highly sensitive quasi-static phenomena, measurement of unsteady wing surface pressures, loads, and accelerations were incorporated into the test procedures to investigate the potential unsteady causes and/or indicators of AWS.”

The initial findings from these tests showed highly unsteady surface pressures indicative of shock oscillation.

Unsteady shock oscillations have been highlighted by Dolling [5] as a problem for steady state methods. The supersonic separated compression ramp pulses at low frequency. The resulting time-averaged surface pressures are smeared due the time averaging of a moving shock. Accurately predicting this flow has eluded CFD researchers for decades. Dolling [5] suggests that better agreement with time-averaged experimental data could be obtained if the CFD simulation included the global unsteadiness of the shock motion, then took a time average. This is the approach that is taken in the current research.

Besides obtaining an improved time-averaged prediction, however, it is also desired to complement unsteady wind tunnel methods[4] with CFD to gain further insight into the potential of the unsteady flow to contribute to the AWS phenomena. The CFD complements the experiments by providing results unaffected by aeroelastic effects, and more detailed flow visualizations.

The baseline case considered is an 8% model of a pre-production F/A-18E with $10^\circ/10^\circ/5^\circ$ flaps (leading-edge flaps/trailing-edge flaps/aileron flaps) at Mach 0.9 and no tails. DES calculations are performed on a baseline and adapted grid and compared to unsteady wind tunnel measurements and RANS models. Although not a comprehensive validation, confidence is built in the DES method for this class of flow.

In order to obtain approval for releasing this paper to the public, quantitative information has been removed from most vertical scales as per guidelines from the Department of Defense.

2.2 Vortex Breakdown

The F-18 High Angle of Attack Research Vehicle (HARV; see Figure 1) has proven to be an excellent source of data for researchers working on high angle of attack flowfields.[6, 7, 8] Extensive flight testing of the HARV has been conducted that provides a rich source of flow visualization, surface pressures, and aeroelastic information. The F-18 utilizes wing leading edge extensions (LEX) to generate vortices which enhance the wing lift, and the twin vertical tails are canted to intercept the strong vortex field and increase maneuverability. At large incidence, the LEX vortices breakdown upstream of the vertical tails, resulting in a loss of yaw control power and severe aeroelastic effects.[9] This tail buffet phenomenon was reduced by using extensive flight tests to design a LEX fence. The ultimate goal of computationally modeling the flowfield shown in Figure 1 would be to accurately simulate the aeroelastic impact of the LEX vortices on the twin vertical tails. The current level of simulation technology, however, has not allowed for accurate prediction

of vortex breakdown, and the unsteady flow downstream of breakdown, at flight Reynolds numbers.



Figure 1: NASA F-18 High Angle of Attack Research Vehicle (HARV).

The specific aim of this work is to test the accuracy and efficiency of DES in predicting vortex breakdown over a full aircraft. This work builds on previous successful work on vortex breakdown over a delta wing[26]. Another goal of the work is to apply adaptive mesh refinement (AMR) to this challenging flow. Computations are made for the F-18C at $\alpha = 30^\circ$, $M_\infty = 0.2755$, and $Re_\infty = 13.9 \times 10^6$ which determine the importance of highly refined grids (including automatic mesh refinement) on the accurate prediction of complex vortical flowfields. Comparisons are made between steady Reynolds-averaged Navier-Stokes (RANS), unsteady Reynolds-averaged Navier-Stokes (U-RANS), and Spalart-Allmaras DES (SADES), and the resulting predictions are compared with available flight test data for the F-18 HARV.

2.3 Flow Solver

The commercial unstructured flow solver *Cobalt* was chosen because of its speed and accuracy. Strang *et al.* [11] validated the numerical method on a number of problems, including the Spalart-Allmaras model (which forms the core of the DES model). Tomaro *et al.* [12] converted the code from explicit to implicit, enabling CFL numbers as high as one million. Grismer *et al.* [13] then parallelized the code, yielding a linear speedup on as many as 1024 processors. Forsythe *et al.* [14] provided a comprehensive testing and validation of the RANS models: Spalart-Allmaras, Wilcox’s $k - \omega$, and Menter’s models. The Parallel METIS (ParMetis) domain decomposition library of Karypis and Kumar [15] and Karypis *et al.* [16] is also

incorporated into *Cobalt*. ParMetis divides the grid into nearly equally sized zones that are then distributed among the processors.

The numerical method is a cell-centered finite-volume approach applicable to arbitrary cell topologies (e.g, hexahedrals, prisms, tetrahdra). The spatial operator uses the exact Riemann Solver of Gottlieb and Groth [17], least squares gradient calculations using QR factorization to provide second-order accuracy in space, and TVD flux limiters to limit extremes at cell faces. A point implicit method using analytic first-order inviscid and viscous Jacobians is used for advancement of the discretized system. For time-accurate computations, a Newton sub-iteration scheme is employed, and the method is second-order accurate in time.

The compressible Navier-Stokes equations were solved in an inertial reference frame. To model the effects of turbulence, a turbulent viscosity (μ_t) is provided by the turbulence model. To obtain k_t (the turbulent thermal conductivity), a turbulent Prandtl number is assumed with the following relation: $Pr_t = \frac{c_p \mu_t}{k_t} = 0.9$. In the governing equations, μ is replaced by $(\mu + \mu_t)$ and k (the thermal conductivity) is replaced by $(k + k_t)$. The laminar viscosity, μ , is defined using Sutherland’s law.

2.4 Reynolds-Averaged Models

In order to provide a baseline for comparison, computations were performed with two of the leading Reynolds-averaged models. The first model used was the Spalart-Allmaras (SA) one-equation model[18]. This model solves a single partial differential equation for a variable $\tilde{\nu}$ which is related to the turbulent viscosity. The differential equation is derived by, “using empiricism and arguments of dimensional analysis, Galilean invariance and selected dependence on the molecular viscosity.” The model includes a wall destruction term that reduces the turbulent viscosity in the log layer and laminar sublayer, and trip terms that provide a smooth transition from laminar to turbulent. For the current research, the trip term was turned off, and the flow assumed fully turbulent.

The second model used was Menter’s Shear Stress Transport (SST) model[19, 20]. The method is a blend of a $k - \epsilon$ and $k - \omega$ model which uses the best features of each model. The model uses a parameter F_1 to switch from $k - \omega$ to $k - \epsilon$ in the wake region to prevent the model from being sensitive to freestream conditions. The implementation used includes a compressibility correction as detailed in Forsythe *et al.* [14].

2.5 Detached-Eddy Simulation

The original DES formulation is based on a modification to the Spalart-Allmaras RANS model[18] such that the

model reduces to its RANS formulation near solid surfaces and to a subgrid model away from the wall[21]. The basis is to attempt to take advantage of the usually adequate performance of RANS models in the thin shear layers where these models are calibrated and the power of LES for resolution of geometry-dependent and three-dimensional eddies. The DES formulation is obtained by replacing in the S-A model the distance to the nearest wall, d , by \tilde{d} , where \tilde{d} is defined as,

$$\tilde{d} \equiv \min(d, C_{DES}\Delta). \quad (1)$$

In Eqn. (1), for the computations performed in this project, Δ is the largest distance between the cell center under consideration and the cell center of the neighbors (i.e., those cells sharing a face with the cell in question). In “natural” applications of DES, the wall-parallel grid spacings (e.g., streamwise and spanwise) are at least on the order of the boundary layer thickness and the S-A RANS model is retained throughout the boundary layer, i.e., $\tilde{d} = d$. Consequently, prediction of boundary layer separation is determined in the ‘RANS mode’ of DES. Away from solid boundaries, the closure is a one-equation model for the sub-grid-scale (SGS) eddy viscosity. When the production and destruction terms of the model are balanced, the length scale $\tilde{d} = C_{DES}\Delta$ in the LES region yields a Smagorinsky eddy viscosity $\tilde{\nu} \propto S\Delta^2$. Analogous to classical LES, the role of Δ is to allow the energy cascade down to the grid size; roughly, it makes the pseudo-Kolmogorov length scale, based on the eddy viscosity, proportional to the grid spacing. The additional model constant $C_{DES} = 0.65$ was set in homogeneous turbulence[22], and was used in the following calculations.

3 Results

3.1 Abrupt Wing Stall

3.1.1 Calculation Details

As previously mentioned, the configuration examined was an 8% scale pre-production F/A-18E with $10^\circ/10^\circ/5^\circ$ flaps set. All of the calculations were carried out on a model with no vertical or horizontal stabilizer (no tails). The force coefficients presented here are compared to a no tails wind tunnel model. Wing surface pressures are compared to a wind tunnel model with tails, however there was seen to be good agreement in surface wing pressures between a model with tails, and that without. The Mach number for all cases was 0.9, and the Reynolds number was 3.8×10^6 per foot, leading to a chord based Reynolds number of 3.98×10^6 . This Reynolds number was set by adjusting the freestream temperature and setting stan-

dard day sea level pressure. In order to compare frequencies and times to unsteady wind tunnel data, the resulting times in the CFD calculations were scaled by the ratio of the CFD freestream velocity to the wind tunnel freestream velocity (a factor of 1.28). The wind tunnel comparisons are from the model tested in NASA Langley’s 16 ft Transonic Tunnel (16TT). The wing was instrumented with both steady and unsteady pressure taps as shown in Figure 2. This paper will focus on the G row (highlighted), since it is directly behind the snag (in the streamwise direction), where the shock induced separated flow occurred furthest forward.

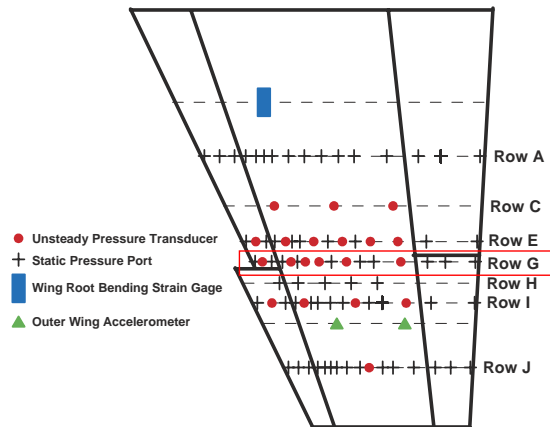


Figure 2: F/A-18E experimental pressure ports.

The grids used were unstructured grids created using the tetrahedral grid generator VGRIDns[23]. The *Cobalt* utility *blacksmith* was used to recombine the high aspect ratio tetrahedra in the boundary layer into prisms. The “Baseline” grid was 7.3×10^6 cells for half the aircraft. The average first y^+ for the grid was 0.2 with a geometric growth rate of 1.25. An adapted grid was created in an attempt to improve on poor DES results on the baseline grid at 9° angle of attack. The utility (*fv2usm*) was used to convert the *Cobalt* solution file to a format readable by RefineMesh (a companion to VGRIDns - see Morton *et al.* [24]). The solution used for adaption was the time averaged solution from a DES 9° angle of attack run. A level of vorticity was selected that contained the separation bubble, and the grid spacing reduced by a factor of 0.6 in each coordinate direction. This should in general lead to $(1/0.6)^3 = 4.63$ times the number of points. However since this reduction in spacing was only applied in a narrowly focused region, the grid only increased from 7.3×10^6 to 9.1×10^6 cells. Cross sections of the “Baseline” and “Adapted” grids are shown in Figure 3. A sample instantaneous DES solution at 9° angle of attack is shown in Figure 4 on the G row. The LES

character of DES is clearly shown - as the grid spacing is reduced, smaller and more turbulence length scales are resolved. This reduces the modeling errors by increasing the resolved turbulence. By comparing Figure 3 to 4, it is also seen that the increased density of points is efficiently placed where needed - in the separation bubble. Although the adaption was carried out at a single angle of attack, the grid was used for the other angles. For lower angles, the separation bubble is further aft, so the adapted region included the separation bubble. For angles higher than 9° , the separation bubble was larger than the adapted region. The adaption was applied only outside the boundary layer cells.

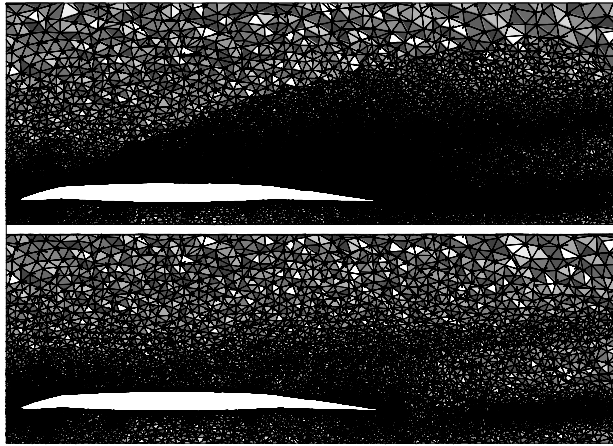


Figure 3: Baseline vs. adapted grid for F/A-18E with no tails.

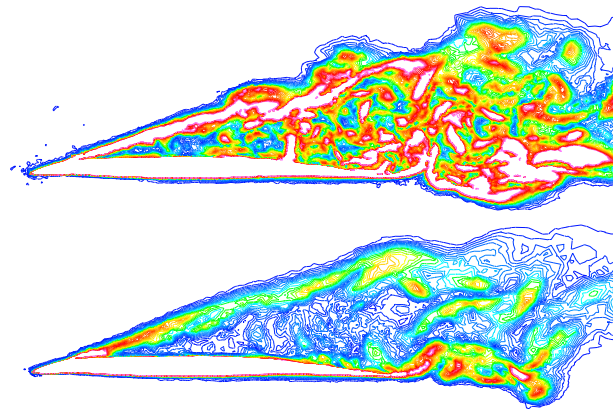


Figure 4: Vorticity contours on the baseline vs. adapted grid for F/A-18E with no tails.

For the RANS calculations, the code was run at a specified maximum global CFL of 1.0×10^6 to accelerate the convergence to steady state. Previous unsteady solutions using RANS models had all failed to obtain any signifi-

cant levels of unsteadiness. Convergence was assessed by monitoring forces and moments during the run. When the change in forces and moments was less than 1% over 500 iterations, the solution was considered converged. This occurred between 2,000 and 4,000 iterations depending on the angle of attack.

DES calculations were of course performed time-accurate. Three Newton subiterations were used, based on previous experience. To ensure a proper choice in timestep, a timestep study was performed on the adapted grid. The timesteps examined were 0.64×10^{-5} , 1.28×10^{-5} , and 2.56×10^{-5} seconds. These timesteps corresponded to non-dimensional (by chord and freestream velocity) timesteps of 0.006, 0.012, and 0.024 respectively. The flow was first initialized by running the middle timestep for 4000 iterations. Then the calculations were run for 8000, 4000, and 2000 iterations respectively over the same length of physical time (0.0512 seconds). Power spectra of the half-aircraft rolling moment for the three timesteps is plotted in Figure 5. There is fairly poor agreement on the power at the low end of the spectra (below 100 Hz) for the smallest timestep. It should be noted, however, that the length of time integrated over is quite small (only able to define 20 Hz), and the low end of the spectra may need longer sampling to define it well. The middle frequency range agrees fairly well for all timesteps (between 100 and 2000 Hz). The largest timestep starts to fall below the others at 2000 Hz. This represents about 20 iterations per cycle, a reasonable value for a second order accurate code. The middle timestep falls off at about 4000 Hz. This middle timestep is used for all the subsequent calculations. It should also be noted that this spectra provides strong evidence that DES is acting in LES mode since there is a broad range of frequencies resolved, and a healthy inertial subrange. For the subsequent DES calculations, the flow was initialized over a time of 0.0512 seconds, then time averages were taken over at least an additional 0.0512 seconds.

3.1.2 Steady/Time-Averaged Results

One of the motivating factors behind using a turbulence resolving method such as DES is to provide a more accurate time-averaged solution, mean lift and drag for example. This has proven true for a broad range of massively separated flows, such as cylinders, spheres, airfoils/forebodies/aircraft at high alpha, but has not been examined on a shock separated flow.

Time averaged-DES lift, drag, and moment coefficients are plotted vs. RANS calculations, and experimental values in Figures 6, 7, and 8 respectively. The experimental results were for the same configuration, i.e. without tails. The DES on the baseline grid follows the lift curve nicely up until 9° , where it drops in lift relative to the experi-

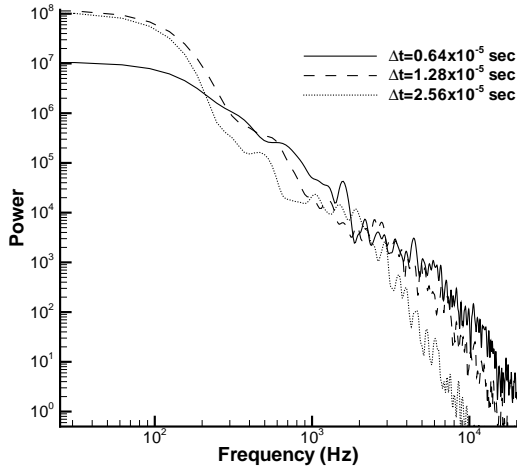


Figure 5: Power spectral density plot of half aircraft rolling moment at various timesteps, 9° angle-of-attack.

ment. This discrepancy is what prompted the creation of the adapted grid, which matched the experiments better. The adapted grid matches the experiments quite well at all angles, with the largest discrepancies at 12° and 16°. This slight error could perhaps be removed/reduced by adapting a grid to the flow solution at these angles, since the adapted grid was tailored to 9°, which has a smaller separation bubble than the higher angles. The Spalart-Allmaras RANS results over predict the lift at all angles, even at the low angles. Parikh and Chung [25] performed SA calculations on an F/A-18E with the same flap settings and picks up the lift break between 9° and 12°, where we don't have calculations. The Menter's SST model captures the low angles better but the lift curve breaks slightly early. The drag curve (Figure 7) shows essentially the same trends — over prediction by SA at all angles, an underprediction by SST near the lift break, and good agreement for the adapted DES.

The pitching moment coefficient (Figure 8) shows the most sensitivity to the model. Since the current grid has no tails, the moment coefficients are quite different than those presented by Parikh and Chung [25]. The adapted DES grid shows quite good agreement throughout the entire angle of attack range. SA underpredicts the moment, while SST overpredicts it at all but the two lowest angles.

To understand the differences between the models, pressure coefficients along the G row are plotted vs. experiments in Figures 9, 10, and 11 for 2°, 9°, and 12° respectively. Figure 9 suggests that experimentally there is separation over the trailing edge flap/aileron at 2°. Adapted DES does a good job of picking up the pressure level on the aileron correctly, although the agreement at

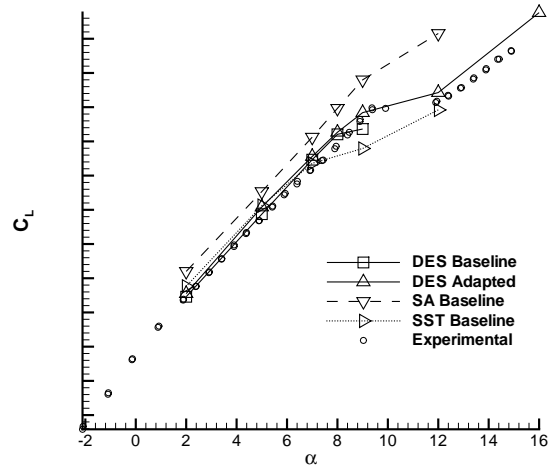


Figure 6: Lift Coefficient vs. alpha for the no tails F/A-18E.

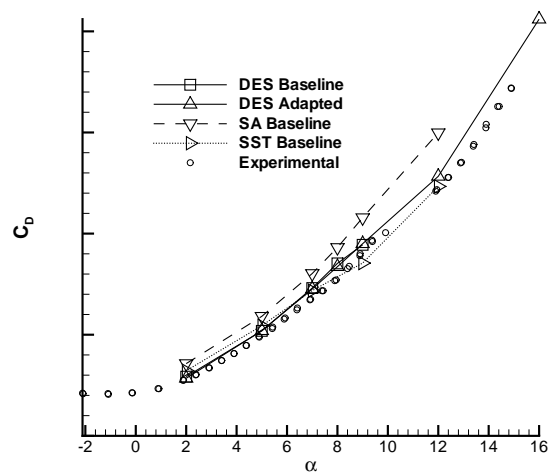


Figure 7: Drag Coefficient vs. alpha for the no tails F/A-18E.

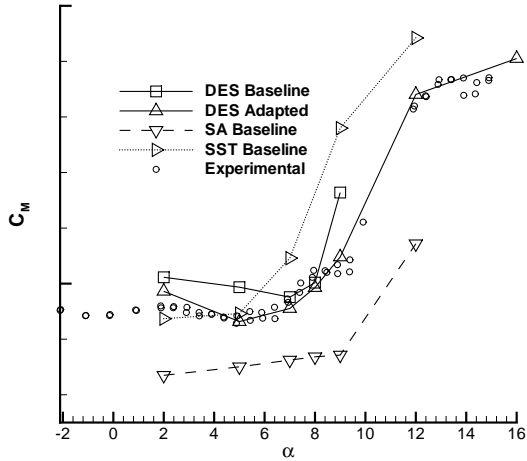


Figure 8: Pitching Moment Coefficient vs. alpha for the no tails F/A-18E.

the trailing edge is not perfect (neither is the pitching moment at this angle). SST only slightly overpredicts the pressure, hence the close but slight overprediction of lift. SA overpredicts the pressure on the flap by a significant amount, which is likely the cause for the overprediction in lift throughout the low angles.

At 9° (Figure 10) the experiments show a smoothly varying pressure distribution from the snag back to about the half chord. Schuster and Byrd [4] showed with unsteady pressure measurements that this pressure distribution occurs due to the time-averaging of an unsteady shock that moves back and forth over the wing. This is certainly a difficult effect for the RANS models to pick up. In this case both SA and SST predict relatively sharp shocks - with SST separating early, and SA late. The DES adapted solution, as will be discussed in the following section, contains a moving shock, that when time-averaged gives a smeared out pressure profile. The time averaged pressures suggest that the unsteady shock stays too far forward compared to the experiments.

At 12° (Figure 11) the flow is separated over the entire chord from the leading edge of the wing. SA overpredicts the pressure (and therefore the lift), while DES and SST match quite well. The fact that SST matches so well here suggests that the errors in pitching moment are arising from a location other than behind the region along the G row.

3.2 Unsteady Results

To assess the accuracy of DES in computing unsteady effects associated with AWS, comparisons are made to the

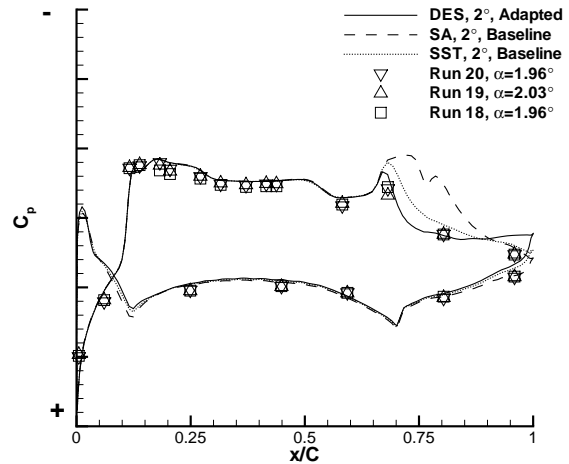


Figure 9: Time-averaged pressure coefficient vs. chord location for the no tails F/A-18E on the G row, 2° angle-of-attack.

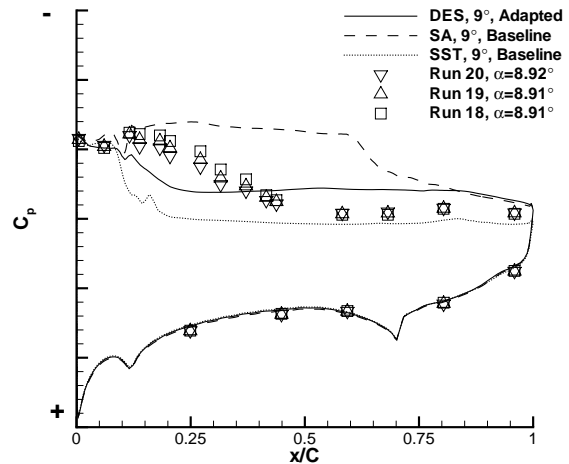


Figure 10: Time-averaged pressure coefficient vs. chord location for the no tails F/A-18E on the G row, 9° angle-of-attack.

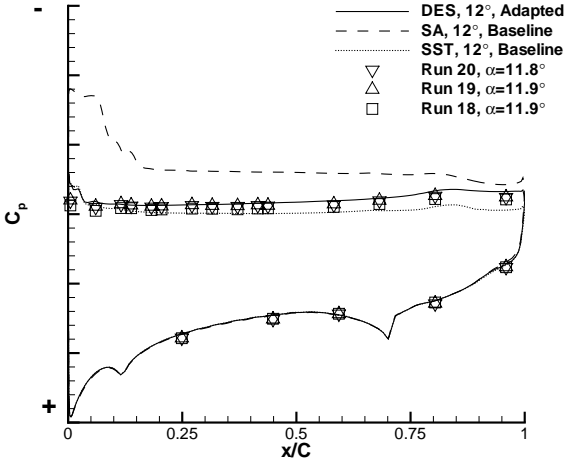


Figure 11: Time-averaged pressure coefficient vs. chord location for the no tails F/A-18E on the G row, 12° angle-of-attack.

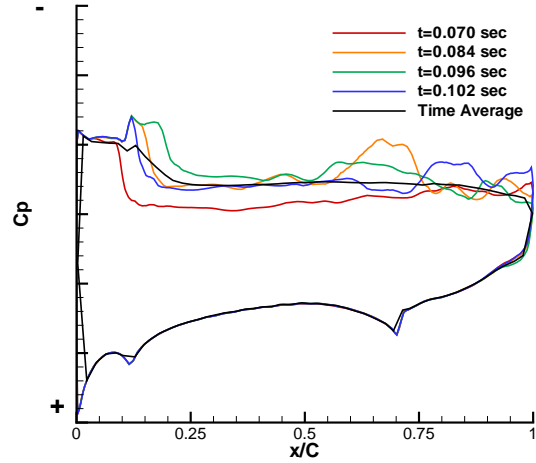


Figure 12: Pressure contours from the DES adapted calculation at four instants in time, and time-averaged at 9° angle of attack

unsteady experimental data of Schuster and Byrd [4]. The effect of the unsteady shock on the mean pressure profile is shown in Figure 12. This plot shows instantaneous pressures at four different times as well as the average pressure for the DES calculation at 9° angle of attack. Although the instantaneous shocks are all sharp, when time averaged a smooth pressure profile results.

Comparisons between the DES calculations and the experiments are shown in Figures 13, 14, and 15. Surface pressures along the G row are plotted, where the experiments had six unsteady pressure taps and ten steady taps. Additionally, there were five steady pressure taps on the bottom of the wing. It was impracticable to store the entire set of CFD results for all timesteps, so the CFD calculations were “tapped” on the G row, and pressures saved every five iterations for subsequent post processing. For the baseline calculations, only the 16 experimental taps on the top of the wing were used. For the refined grid calculations, 100 equally spaced points on the G row were tapped on both upper and lower surfaces to allow for more detailed analysis of the shock motion. Pressure statistics were calculated from the experiments and CFD, including the mean, standard deviation, and the minimum and maximum values of pressure. For both the CFD and experiments, any individual pressure that fell outside a three-standard-deviation (3σ) band about the computed mean was excluded for the maximum or minimum pressure value. For the CFD calculations this mainly smoothed out the min and max coefficients of pressure behind the shock location.

Statistics at 7° are plotted for the baseline grid in Fig-

ure 13. The five experimental mean pressures near the bottom of the plot are from the lower wing surface where the CFD pressures were not examined. The agreement in the mean, maximum, and minimum pressures on the top surface is quite good. The shock in the CFD is slightly too far forward and the range of pressure oscillations is slightly underpredicted.

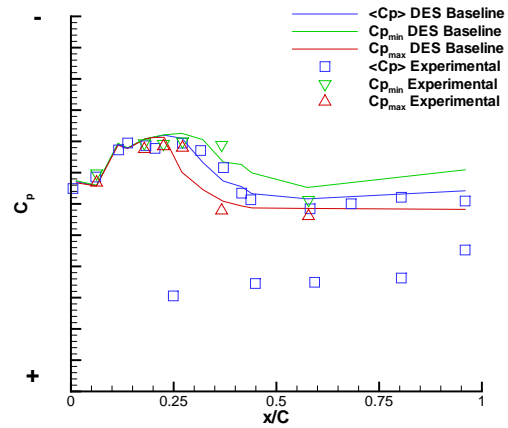


Figure 13: Min, Max, and average pressure coefficient on the G row, 7° angle-of-attack.

Statistics at 9° are plotted for the baseline and adapted grids in Figure 14. The oscillations in the baseline grid were underpredicted and the shock too far forward. The adapted grid helped improve the results - increasing the

amount of shock oscillation, and moving the mean shock location further aft. These improvements showed up as an improved mean lift prediction as previously discussed.

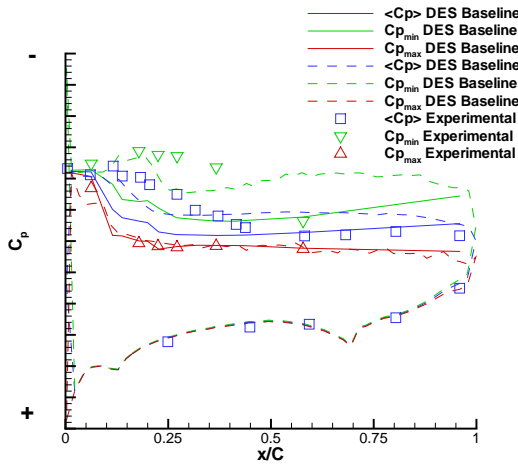


Figure 14: Min, Max, and average pressure coefficient on the G row, 9° angle-of-attack.

Statistics at 12° are plotted for the adapted grid in Figure 15. The agreement of the maximum, minimum, and average pressure to the experiments is quite good. The pressures had only weak oscillation since the flow was fully separated, and there was no shock oscillation as in the 7° and 9° cases.

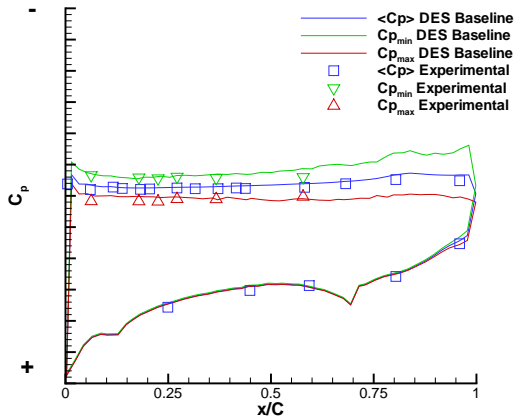


Figure 15: Min, Max, and average pressure coefficient on the G row, 12° angle-of-attack.

To determine if unsteady shock oscillation could be a contributor to the AWS phenomenon, half-aircraft rolling moment is next examined in Figure 16. The half aircraft rolling moment was calculated by taking the rolling moment of the half-aircraft and non-dimensionalizing by the

span and half the wing area. This of course leads to a non-zero mean coefficient, but a feel for the level of unsteadiness in rolling moment can be obtained by comparing the peak to peak differences. The differences in peaks in Figure 16 although not shown on the axis was considered “significantly large” and a potential contributor to triggering an AWS event. A small slice of this rolling moment plot is shown in Figure 18 with flow visualizations at seven instants in time. Figure 18a corresponds to a large rolling moment, since it has low lift, which would produce a right roll. In Figure 18b, a tiny separation bubble forms on the snag, further reducing lift and increasing the rolling moment. The shock then moves back in Figure 18c-e until the lift is at a maximum, and the rolling moment is at a minimum. From that point it moves forward in Figure 18f-g. The cycle can then repeat.

What is significant is that this shock motion causes a rolling moment change at a low frequency - approximately 25 Hz. This would scale to 2Hz for the full scale aircraft. This was however only a half aircraft calculation, so care must be taken in drawing conclusions from this plot. The net rolling moment will depend on the flow on the other wing. It would in general be possible for the shock locations on the other wing to be perfectly correlated, and therefore have zero rolling moment. Given the chaotic nature of the flow, however, this seems extremely unlikely. Another possibility is that the shocks on both wings oscillate in a very narrow frequency range, which could give rise to a very low beat frequency. Schuster and Byrd [4], however, shows that the shock motion occurs in a broadband frequency range so this would not be expected.

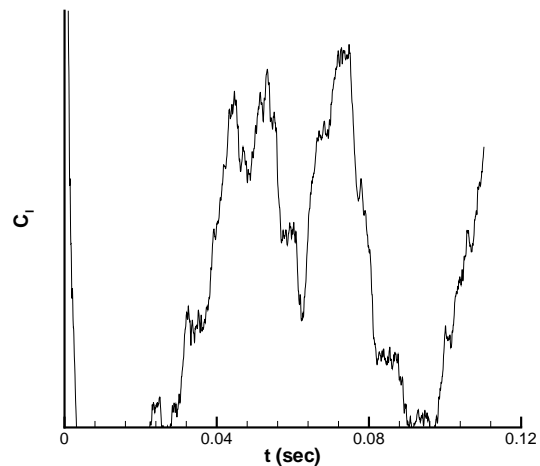


Figure 16: Rolling moment vs. time for half aircraft calculation (no tails).

In order to provide conclusive evidence that the low frequency shock motion could lead to large low frequency rolling moments on a full aircraft, the half-aircraft adapted grid was mirrored around the plane of symmetry leading to an 18.2×10^6 cell grid. This grid was then run in the same manner as previous calculations, at 9° angle of attack. The resulting rolling moment is shown in Figure 17, with the same scale as Figure 16, but centered on zero. The magnitude and frequency of the full aircraft calculation seems to match up fairly closely to the half aircraft calculation. The first 1/3 of the time represents the initial start up of the flow solution and would normally be discarded. However, it is interesting to see that there is a growth of lateral instabilities despite the grid and initial flowfield symmetry. This initial asymmetry must come from slight asymmetries in the flow solver (asymmetries in the grid partitioning, ordering of the grid, machine roundoff, etc) that are then amplified by the unstable nature of the flow. If these initial asymmetries were not present then it would be necessary to provide some flow field asymmetry in the initial conditions. Comparisons are not made to unsteady rolling moments from the experiments since they were believed to be polluted by aeroelastic effects since the frequency of rolling moment oscillation correlated with one of the aeroelastic modes of the model, rather than frequencies from the surface pressures. However, the magnitude of the maximum rolling moment of the CFD calculation was similar to that seen in the wind tunnel.

locity are an indicator of the separated region. The shock on the left side starts further back in Figure 19a, giving a large positive right rolling moment. As this shock moves forward, the rolling moment moves towards zero in Figure 19b. Then the right shock moves aft in Figure 19c, giving a large negative rolling moment.

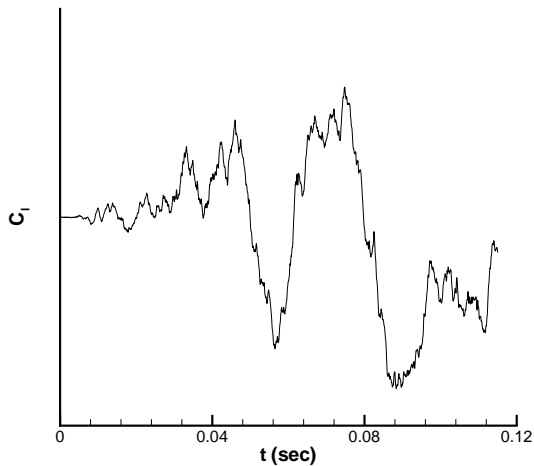


Figure 17: Rolling moment vs. time for full aircraft calculation (no tails).

Flow visualizations are also provided for this calculation in Figure 19, with a zoomed in region of the rolling moment plot. These isosurfaces of zero streamwise ve-

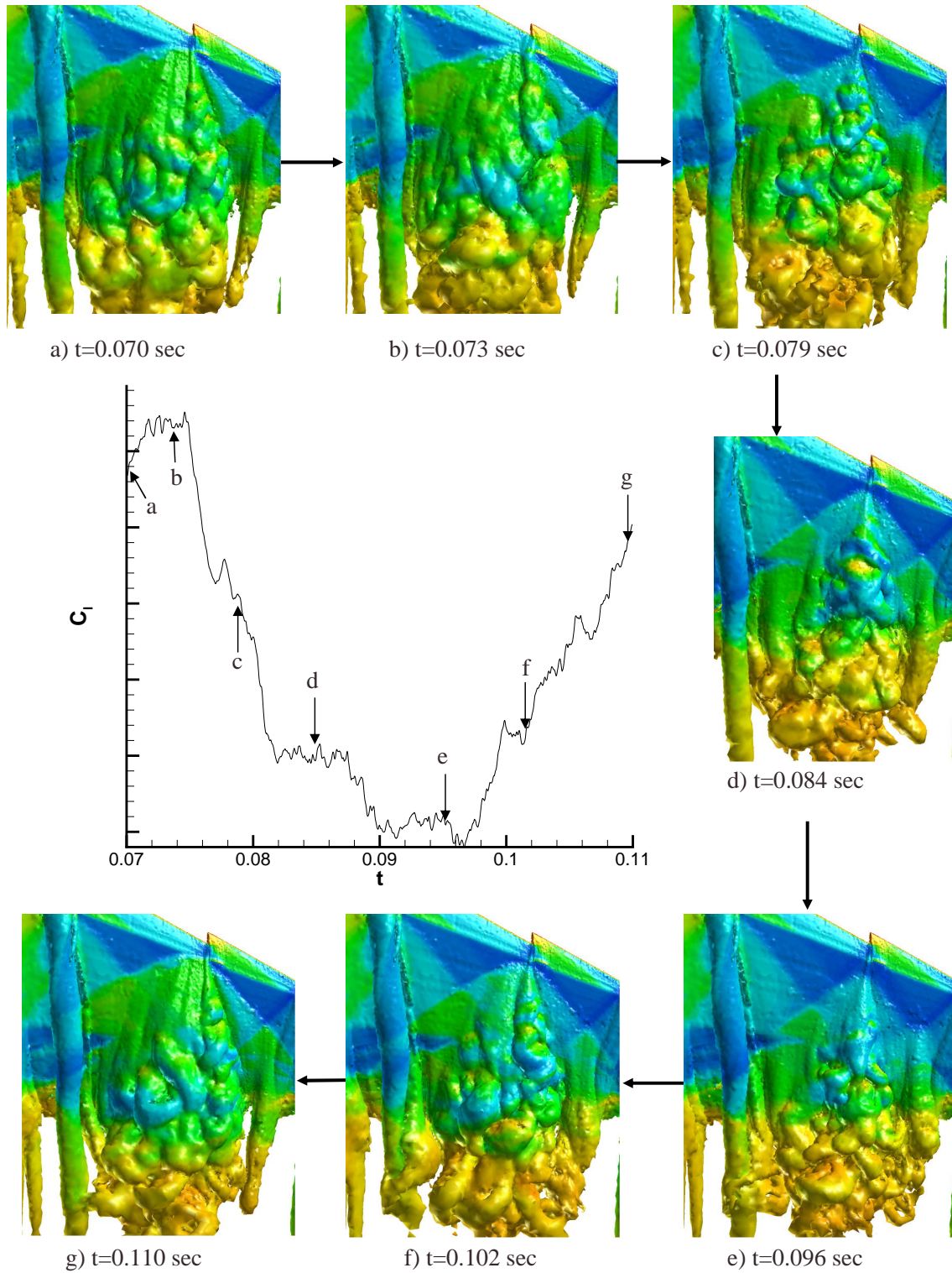


Figure 18: Plot of Rolling moment vs. time and flow visualizations at specific times – half aircraft. Flow visualizations are isosurfaces of vorticity colored by pressure (no tails).

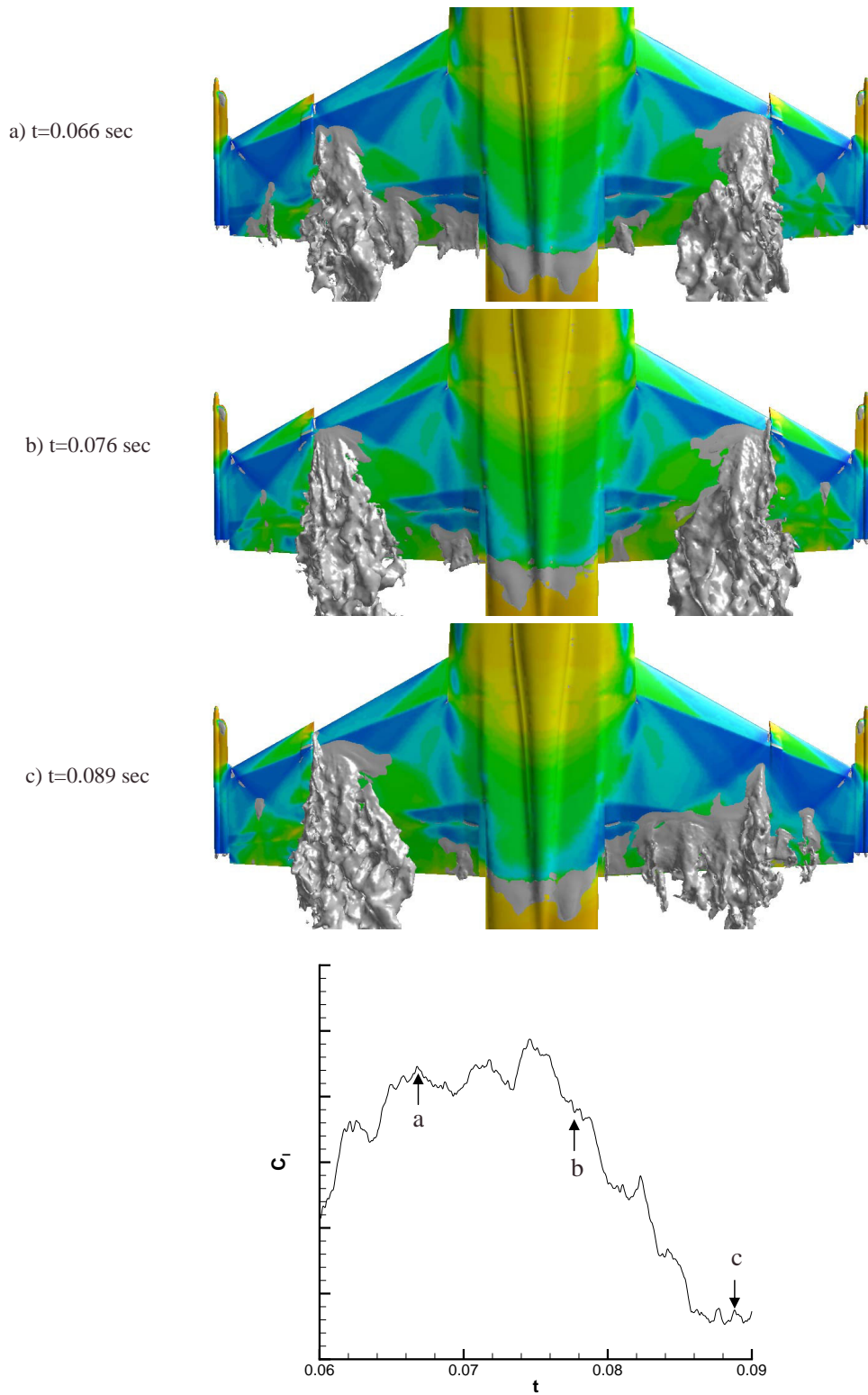


Figure 19: Plot of Rolling moment vs. time and flow visualizations at specific times – whole aircraft. Flow visualizations are isosurfaces of vorticity colored by pressure (no tails).

3.3 Vortex Breakdown

3.3.1 Calculation Details

All F-18C cases were run at 30° angle-of-attack, a Mach number of 0.2755, and a standard day at 20,000 feet. The resulting Reynolds number was 13.9×10^6 based on the mean aerodynamic chord. The baseline grid of 5.9 million cells was generated with VGRIDns[23]. Steady SA-RANS, unsteady SA-RANS, and unsteady SADES turbulence model simulations were performed on the baseline grid. A time-averaged SADES solution was used to produce an AMR grid with 6.2 million cells by following the approach outlined for the delta wing above. All time-accurate simulations were run for over 10,000 iterations with second-order temporal and spatial accuracy, three Newton sub-iterations, and a time step of 0.0005 seconds. The steady SA-RANS simulation was run for 3000 iterations with first-order temporal and second-order spatial accuracy, one Newton sub-iteration, and a CFL number of 1 million.

Figure 20 depicts a top view of the surface mesh and Figure 21 depicts a cross-plane at a station 410 inches aft of the origin for both the baseline grid and the AMR grid. It is obvious from Figure 21 that the AMR grid has enhanced resolution in the core of the LEX vortex, the separated region over the wing, at the wingtip pylons, and the under wing pylons. These enhanced grid regions are due to the AMR based on a vorticity iso-surface corresponding to separation regions at these locations and due to the vorticity in the LEX vortex core.

3.3.2 Results

In Figure 22, cross-planes of streamwise vorticity at two streamwise locations are shown for the baseline grid solution (left) and the AMR grid solution (right) for a particular instant in time. For ease of comparison, the sense of the vortex is redefined to match the color scheme on the left wing with the right wing even though these vortices rotate in opposite directions. The pre-breakdown cross-plane at 360 inches aft of the origin shows that the AMR grid solution provides better definition of the complex vortical flowfields encountered at this angle of attack. A primary LEX vortex core is observed (red) over the top of a secondary vortex (blue), as well as a wing vortex (blue) is observed just outboard of the LEX secondary vortex. Neither this wing vortex nor the LEX vortex are as well defined on the baseline grid as the AMR grid at this pre-breakdown location. Since the flowfield aft of breakdown varies tremendously with time and the cross-planes at station 410 in. are instantaneous, no conclusions can be made for the accuracy of the AMR grid solution versus the baseline grid solution.

To determine the location of vortex breakdown for the

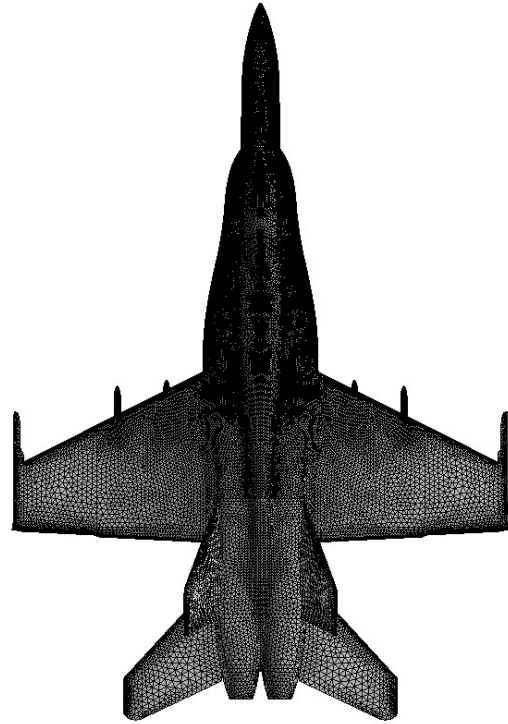


Figure 20: Top view of the baseline grid (5.9 million cells).

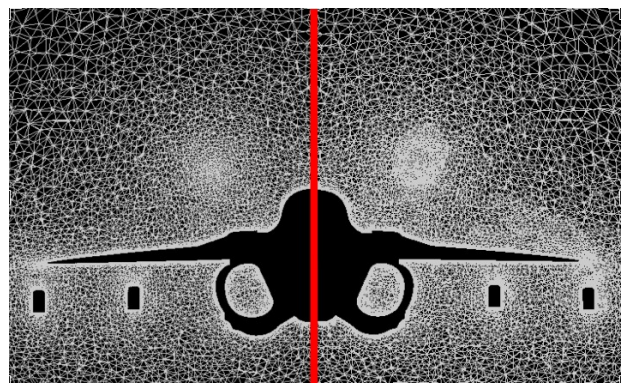


Figure 21: Baseline grid of 5.9 million cells (left) and AMR grid of 6.5 million cells (right) at a station 410 inches aft of the origin.

F-18C at 30° angle-of-attack, the streamwise velocity component along the core of the vortex is plotted versus the streamwise location (Figure 23). A common definition of vortex breakdown is the location where the streamwise velocity component is zero in the core. It should first be noted that both the steady and unsteady SA-RANS simulations produced no vortex breakdown. This inability of commonly used turbulence models to compute a solution with breakdown is well documented in the literature and is due to the large amount of eddy-viscosity these models put into the core of vortices[26]. Several researchers have proposed fixes to these turbulence models by incorporating some form of a streamline curvature and rotation correction. The disadvantage of this approach is the fact the simulation may still be operating in a RANS mode and compute solutions that are relatively steady post-breakdown as opposed to an LES approach that resolves the eddies that produce the unsteadiness. It is clear in Figure 23 that the DES method does not suffer from the same problem as the RANS method due to the fact that eddy viscosity is computed based on sub-grid scale turbulence, automatically minimizing the amount eddy-viscosity that is placed in the core of vortices. The baseline grid solution shows vortex breakdown occurring at 430 inches aft of the origin and the AMR grid shows vortex breakdown occurring at 475 inches aft of the origin. It should be noted that these are instantaneous solutions and the vortex breakdown position can vary up to 10%.

Figure 24 depicts the power spectral density (PSD) plot of an outboard tail pressure port. Figure 24 again shows the inability of standard RANS methods to compute the unsteady flowfield necessary to provide realistic loads data to be used in an aeroelastic analysis. A five order of magnitude increase in power is observed for the DES solutions as compared to the RANS solution. Although the difference is not as dramatic between the baseline grid SADES solution and the AMR grid SADES solution, there is still a respectable improvement in power for the frequency range 0.8 to 8 and the modest increase in cells (5%) of the AMR grid.

Figure 25 shows an isometric view of the F-18C with an iso-surface of vorticity equal to $750s^{-1}$ colored by pressure for the unsteady SA-RANS, SADES baseline grid, and SADES AMR grid solutions. Both the instantaneous solutions and the time-averaged solutions after 10,000 iterations are provided. In Figure 25a and b it is apparent that the SA-RANS solution does not physically represent the vortex observed in flight and depicted in Figure 1 for the F-18 HARV. It is also interesting to note the instantaneous and time averaged solutions are essentially equivalent for the SA-RANS solution. On the other hand, both SADES solutions are in excellent qualitative agreement with the vortex breakdown observed in Figure 1. The SADES solutions also capture the separation

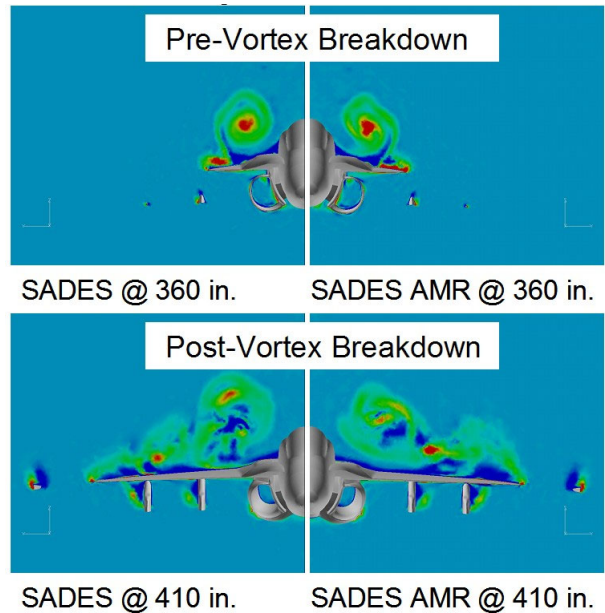


Figure 22: Cross-planes of vorticity at two stations (pre- and post-breakdown) on the F-18C for the baseline grid (left) and the AMR grid (right).

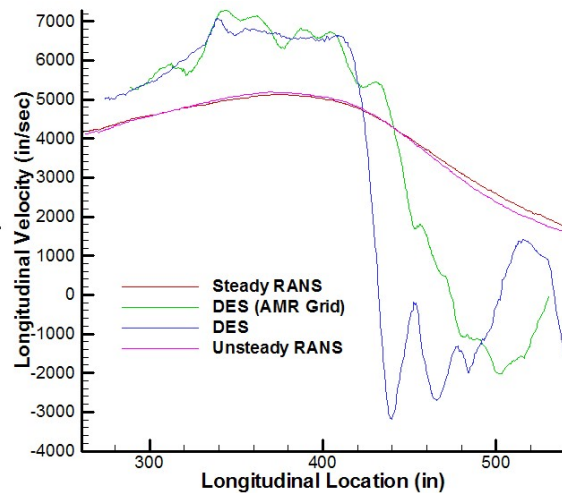


Figure 23: Cross-planes of vorticity at two stations (pre- and post-breakdown) on the F-18C for the baseline grid (left) and the AMR grid (right).

over the wing and horizontal tail. Careful examination of Figs. 12e and f show that the AMR grid solution captures small scale structures surrounding the LEX vortex better, consistent with earlier delta wing case. Figures 12d and f display the time average of the SADES solutions. Both figures show evidence of the vortical substructures in the time average solution. Also, the time average of the AMR grid shows an iso-surface that extends further aft. By compiling a series of these snapshots, a movie can be created that shows the unsteady behaviour of the post-breakdown windings, the pre-breakdown substructures, and the separated flow regions. It is clear from the simulation that the tails are in a very unsteady environment contributing to the fatigue issues well documented for the F-18 without the LEX fence. It is also clear that the industry standard RANS methods for these high Reynolds number flows are completely inadequate for obtaining unsteady loads on tails due to vortex breakdown.

In order to lend credibility to the F-18C SADES solutions with and without AMR of the current study, comparison is made with the F-18 HARV flight test data[6, 7, 8]. It is important to note the differences in the F-18C grid and the actual F-18 HARV. The F-18C of the current study has leading edge flaps set to 0 degrees deflection whereas the F-18 HARV leading edge flaps were deflected down 33 degrees. The trailing edge flaps were set to 0 degrees deflection for both the F-18C and the F-18 HARV. The F-18C has a diverter slot that goes through the upper surface of the LEX creating a jet-like flowfield above the LEX but was sealed over for the F-18 HARV. Also, the under-wing pylons are on the F-18C but were taken off of the F-18 HARV. Finally, the F-18C has rigid tails in the simulations but they are fairly flexible in the F-18 HARV with tip deflections on the order of a few percent of the tail root chord. Although these differences in configuration are not trivial, comparison can still be made to determine the qualitative agreement with the flight test.

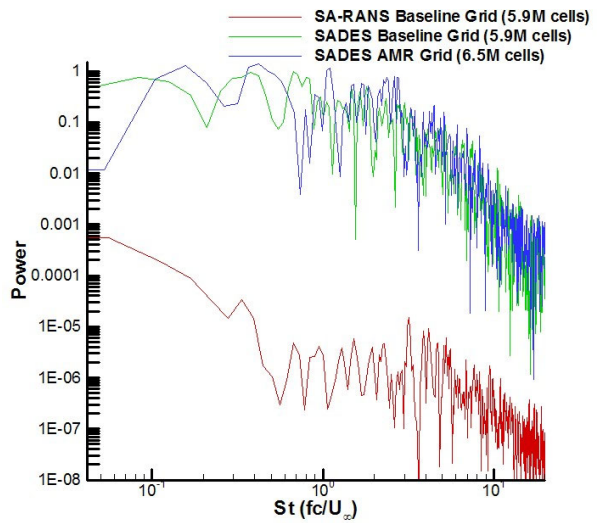


Figure 24: MATLAB power spectral density analysis of the outboard tail pressure port at the 10% chordwise and 50% spanwise position for the SA-RANS and SADES baseline grid solution and the SADES AMR grid solution.

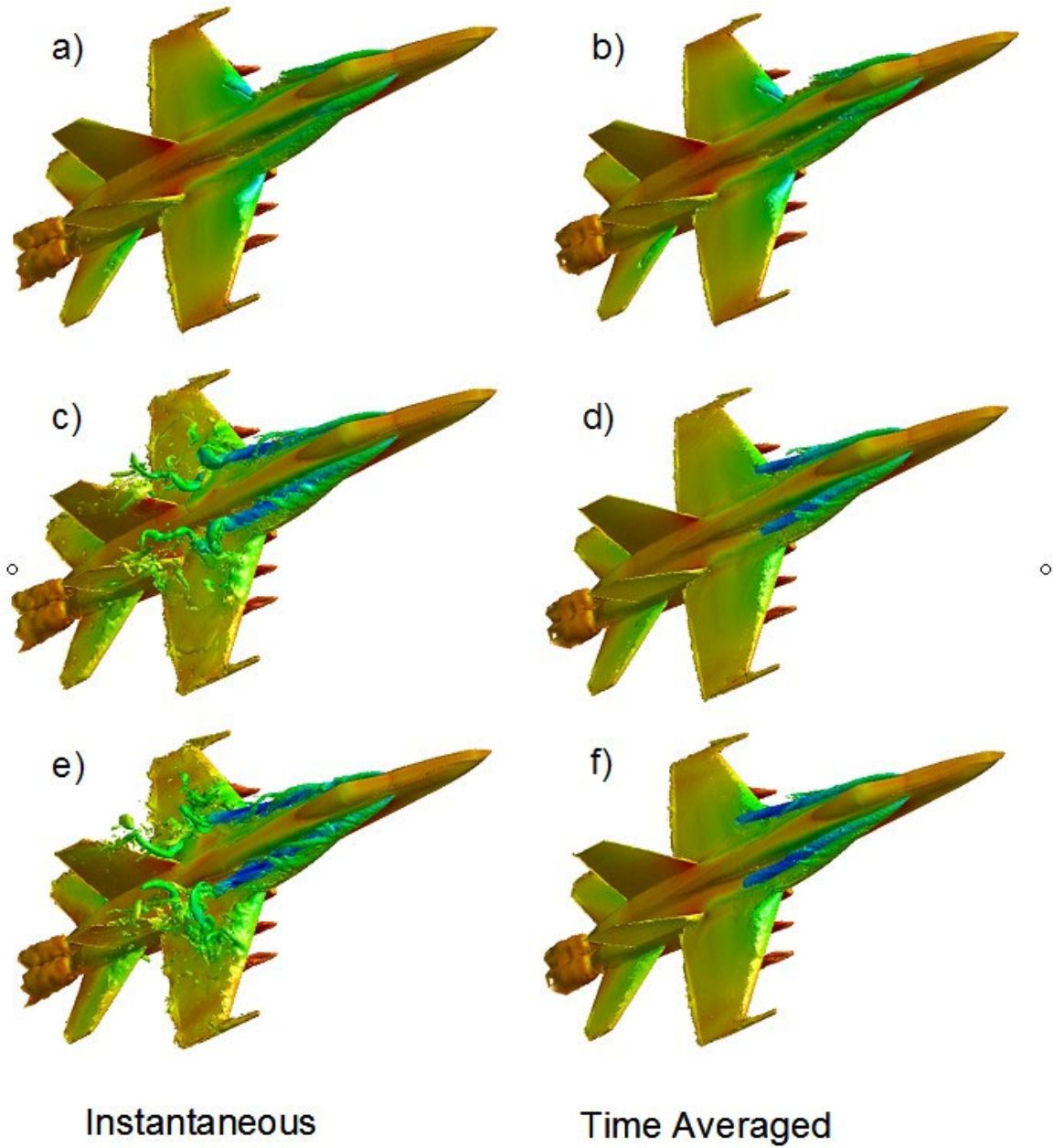


Figure 25: Isometric views of the F-18C at $\alpha = 30^\circ$, $Re_c = 13.9 \times 10^6$, leading and trailing edge flaps set to 0° and the diverter slot present. a, c, and e depict instantaneous views of the SA-RANS, SADES baseline grid, and SADES AMR grid solution, respectively. b, d, and f depict solutions time averaged after 10,000 time steps for the the SA-RANS, SADES baseline grid, and SADES AMR grid solution, respectively.

Figure 26 displays the lift force in pounds of the simulation as a function of time. The steady and unsteady RANS simulations converge quickly to the same lift force of 37,175 lbs with a variation of plus or minus 20 lbs and both SADES solutions have a mean of 35,400 lbs plus or minus 1,800 lbs. Therefore, the SA-RANS simulations are 5% higher than the SADES solutions and relatively steady. If the F-18C grid was modified to include the -33° leading-edge flap extension, both the SA-RANS and SADES simulations would have a higher lift, due to the increased camber of the wing, possibly moving the SADES solutions closer to the flight test. It is interesting to note that the F-18 HARV was fairly trimmed with a weight of 37,193 lbs, indicating that the simulations are qualitatively correct.

Figure 27 shows the PSD of the F-18 HARV outboard vertical tail pressure port in the same location as the simulation pressure port of Figure 24. Although the power is not of the same magnitude, the frequency roll off is very similar to the SADES grid solutions presented in Figure 24. The Strouhal frequency at the peak of both the SADES and flight test is approximately equal to 1.

Finally, Figure 28 is a well known plot in the literature of the streamwise location of the LEX vortex breakdown as a function of angle-of-attack[7]. For the 30° angle-of-attack of interest in this study, vortex breakdown occurs between 40% and 50%. The location of breakdown observed in Figure 23 for the simulations is at 60%. This discrepancy is not surprising when considering the fact that the diverter slot is covered up on the F-18 HARV. Mitchell *et al.* [27] demonstrated that along the core blowing from the surface can move the breakdown position aft. The jet-like behavior of the diverter slot could be acting like a vortex breakdown flow control device, explaining the aft position of vortex breakdown for the F-18C with a diverter slot.

3.4 Concluding Remarks

3.4.1 Abrupt Wing Stall

In summary, Detached-Eddy Simulation has been applied to the pre-production F/A-18E with $10^\circ/10^\circ/5^\circ$ flap set with comparison to steady and unsteady experimental measurements and leading RANS models. Comparisons were made to experimental surface pressures (both time-averaged and steady) and mean force coefficients. Solution based adaptation was used to improve the simulations. Unsteady rolling moments were observed on both half and full aircraft simulations due to unsteady shock motions.

The mean flow predictions on the adapted grid were seen to be in excellent agreement to the experiments, showing a slight improvement over the SST RANS model,

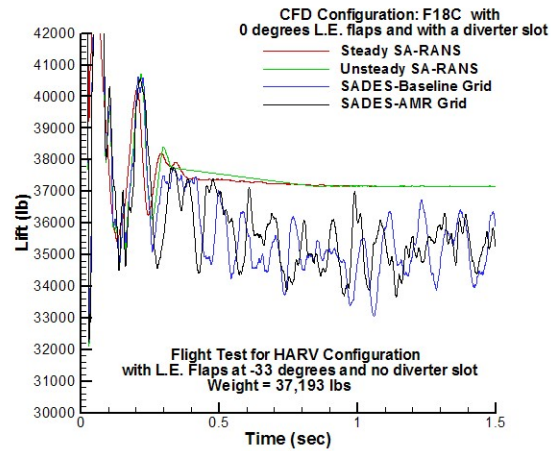


Figure 26: Lift as a function of time for the F-18C at $\alpha = 30^\circ$, $Re_c = 13.9 \times 10^6$, leading and trailing edge flaps set to 0° and the diverter slot present. Steady SA-RANS, unsteady SA-RANS, and unsteady SADES solutions are provided for the baseline grid and an SADES solution is provided for the AMR grid.

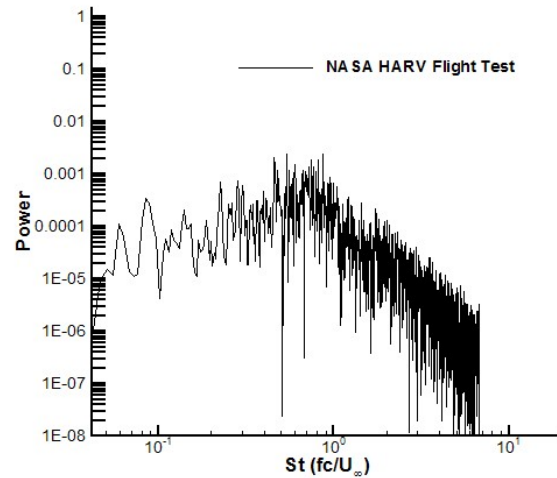


Figure 27: MATLAB power spectral density analysis of the outboard tail pressure port at the 10% chordwise and 50% spanwise position for flight 198 of the NASA HARV F-18.

and a larger improvement over the SA RANS model.

Comparisons to unsteady pressures built confidence in the accuracy of DES for this class of flows, but highlighted a need for longer time-averaging. Current computational speeds put the wind tunnels far ahead in their ability to look at the relatively low frequency shock oscillation associated with this flow. As computer speeds increase this gap will naturally narrow. Calculations on both half and full span aircraft showed large oscillations in rolling moment at low frequency (close to 2Hz when scaled to full scale). This supports the conclusion from the unsteady experiments[4]: “This is significant since the combination of large-scale shock motion and low frequency provide a potential triggering mechanism for lateral instabilities, such as wing drop, which probably could not be effectively damped by the automatic flight control system.” Because the CFD calculations were for a completely rigid aircraft, there is strong support of the conclusion that “the unsteady aerodynamics experienced on the F/A-18E model at AWS conditions are not a direct result of the structural vibrations encountered in the wind tunnel.”[4]

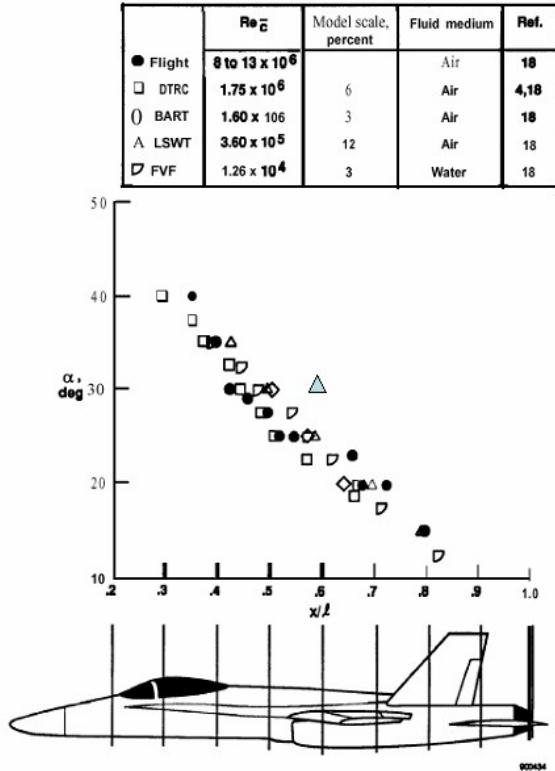


Figure 28: Streamwise LEX vortex breakdown position as a function of angle of attack extracted from [7]. SADES AMR grid solution vortex breakdown location plotted with the flight test and experimental data for comparison.

3.4.2 Vortex Breakdown

The combined SADES and AMR grid approach was demonstrated on an F-18C to determine if the unsteady tail loads could be simulated. As was the case in previous delta wing work, the AMR F-18C grid SADES solution showed an improvement in capturing small scale features of the LEX vortex as compared to the baseline grid SADES solution. Also, an improvement in the power associated with a range of frequencies was demonstrated for the SADES AMR grid solution over the baseline grid solution, consistent with the delta wing analysis. In all cases the SA-RANS solutions proved completely inadequate for computing vortex breakdown for a flight vehicle at high Reynolds number.

Flight test data from the NASA HARV program was used to show the solutions were reasonable even though the aircraft configurations were different. Qualitative agreement between the SADES solutions and the HARV data was obtained for the lift and the vortex breakdown position. A recommendation for future research is to create an F-18C grid that is a closer match to the HARV by moving the leading-edge flap to a -33° position, close off the diverter slot, and eliminate the under-wing pylons.

4 Significance to DoD

Currently, fighter development is under close scrutiny due to ever increasing acquisition costs. The Joint Strike Fighter program incorporated a primary requirement of low cost in their acquisition strategy and have achieved

partial success by pushing the technology of “virtual manufacturing,” or incorporation of modeling and simulation in the manufacturing process. Although, this has helped their program move towards the cost goal, there are other areas that modeling and simulation can play a significant role in reducing the overall acquisition cost.

It is a well known fact that major changes to the airframe after the first air vehicle is produced drives the program cost up significantly. This is due to the necessary retooling, retraining, and recertification through ground and flight test. A large portion of the redesign efforts in fighter aircraft programs are due to the low-order aerodynamic modeling being used as “state of the art” in aircraft design by the major manufacturers.

There are three major fighter aircraft acquisition programs at various phases in the acquisition cycle, the Joint Strike Fighter, the F-22, and the F/A-18E and F. All of these aircraft programs seek to fly with maneuverability superior to other nations fighters. The desire for increased maneuverability forces them to fly in conditions where very complicated aerodynamic-flight mechanic and aerodynamic-structural coupling phenomena are prevalent. Also, a credible tool to model the vehicle in these conditions does not exist in industry and must be developed if the acquisition costs are to be reduced.

5 Systems Used

1. hpc09.asc.hpc.mil – Compaq ES45
2. tempest.mhpc.hpc.mil – IBM P3

6 CTA

Computational Fluid Dynamics (CFD)

Acknowledgments

The authors wish to express their gratitude to the Office of Naval Research (ONR) and the Air Force Office of Scientific Research (AFOSR) for sponsoring this research. We also gratefully acknowledge the support of Bill Strang of Cobalt Solutions for his support of this project. The advice of the rest of the abrupt wing stall team greatly aided the focus and direction of the work. We would also like to say thanks to Dr Shahyar Pirzadeh for his help with the AMR software and Dave Fisher and Al Bowers of the NASA Dryden Flight Research Center for their invaluable assistance with the F-18 HARV flight test data. This work could not have been accomplished without the support of the ASC Major Shared Resource Center of HPCMO, The Maui High Performance Computing Center and the US-AFA Modeling & Simulation Resource Center.

References

- [1] Forsythe, J. R., Squires, K. D., Wurtzler, K. E., Spalart, P. R., “Detached-Eddy Simulation of Fighter Aircraft at High Alpha,” *AIAA 02-0591*, January 2002.
- [2] Squires, K.D., Forsythe, J.R., Morton, S.A., Strang, W.Z., Wurtzler, K.E., Tomaro, R.F., Grismer, M.J. and Spalart, P.R., “Progress on Detached-Eddy Simulation of massively separated flows”, *AIAA 02-1021*, January 2002.
- [3] Hall, R., Woodson, S., “Introduction to the Abrupt Wing Stall (AWS) Program,” *AIAA 03-0589*, Jan 2003.
- [4] Schuster, D., Byrd, J., “Transonic Unsteady Aerodynamics of the F/A-18E at Conditions Promoting Abrupt Wing Stall,” *AIAA 03-0593*, Jan 2003.
- [5] Dolling, D., “Problems in the Validation of CFD Codes Through Comparison with Experiments,” *AGARD Symposium on Theoretical and Experimental Methods in Hypersonic Flows, CP-514*, AGARD, 1993, pp. 19.1–19.15.
- [6] Lee, B.H.K., “Vertical Tail Buffeting of Fighter Aircraft,” *Progress in Aerospace Sciences* **36**, 193-279, 2000.
- [7] Fisher, D., Del Frate, J.H., and Zuniga, F.A., “Summary of In-Flight Flow Visualization Obtained From the NASA High Alpha Research Vehicle,” NASA TM-101734, January 1991.
- [8] Ames Research Center Dryden Flight Research Facility, “High Alpha Research Vehicle Phase II Flight Report, Flight 197-199” HA94-70-660, February 1994.
- [9] Murman, S.M., Rizk, Y.M, Cummings, R.M., and Schiff, L.B., “Computational Investigation of Slot Blowing for Fuselage Forebody Flow Control,” *Aircraft Design*, **2**, pp. 45-63, 1999.
- [10] Squires, K.D., Forsythe, J.R. and Spalart, P.R., “Detached-Eddy Simulation of the Separated Flow Around a Forebody Cross-Section”, *Direct and Large-Eddy Simulation IV*, ERCOFTAC Series – Volume 8, B.J. Geurts, R. Friedrich and O. Metais, editors, Kluwer Academic Press, pp. 481-500, 2001.
- [11] Strang, W. Z., Tomaro, R. F, Grismer, M. J., “The Defining Methods of Cobalt₆₀: a Parallel, Implicit, Unstructured Euler/Navier-Stokes Flow Solver,” *AIAA 99-0786*, January 1999.

- [12] Tomaro, R.F., Strang, W. Z., and Sankar, L. N., "An Implicit Algorithm for Solving Time Dependent Flows on Unstructured Grids," *AIAA 97-0333*, January 1997.
- [13] Grismer, M. J., Strang, W. Z., Tomaro, R. F. and Witzeman, F. C., "Cobalt: A Parallel, Implicit, Unstructured Euler/Navier-Stokes Solver," *Advances in Engineering Software*, Vol. 29, No. 3-6, pp. 365—373, 1998.
- [14] Forsythe, J.R., Strang, W., Hoffmann, K.A., "Validation of Several Reynolds-Averaged Turbulence Models in a 3D Unstructured Grid Code," *AIAA 00-2552*, June 2000.
- [15] Karypis, G., and Kumar, V., *METIS: Unstructured Graph Partitioning and Sparse Matrix Ordering System Version 2.0*. University of Minnesota, Department of Computer Science, Minneapolis, MN 55455, July 1997.
- [16] Karypis, G., Schloegel, K., and Kumar, V., *ParMETIS: Parallel Graph Partitioning and Sparse Matrix Ordering Library Version 1.0*. University of Minnesota, Department of Computer Science, Minneapolis, MN 55455, July 1997.
- [17] Gottlieb, J.J., Groth, C.P.T., "Assessment of Reimann Solvers for Unsteady One-Dimensional Inviscid Flows of Perfect Gases", *Journal of Computational Physics*, **78**, pp. 437-458, 1988.
- [18] Spalart, P.R. and Allmaras, S.R., 1994, "A One-Equation Turbulence Model for Aerodynamic Flows," *La Recherche Aerospatiale* **1**, pp. 5-21.
- [19] Menter, F.R., 1992, "Improved Two-Equation $k - \omega$ Turbulence Models for Aerodynamic Flows," *NASA-TM-103975*.
- [20] Menter, F.R., 1994, "Two-Equation Eddy-Viscosity Turbulence Models for Engineering Applications," *AIAA Journal*, 32(8), pp 1598–1605.
- [21] Spalart, P. R. , Jou W-H. , Strelets M. , and Allmaras, S. R., "Comments on the Feasibility of LES for Wings, and on a Hybrid RANS/LES Approach," *Advances in DNS/LES, 1st AFOSR Int. Conf. on DNS/LES*, Aug 4-8, 1997, Greyden Press, Columbus Oh.
- [22] Shur, M., Spalart, P. R., Strelets, M., and Travin, A., "Detached-Eddy Simulation of an Airfoil at High Angle of Attack, 4th Int. Symp. Eng. Turb. Modelling and Measurements, Corsica, May 24-26, 1999.
- [23] Pirzadeh, S., "Three-dimensional Unstructured Viscous Grids by the Advancing Layers Method," *AIAA Journal*, V. 34, pp. 43-49.
- [24] Morton, S., Forsythe, J., Cummings, R., Steenman, M., "DES Grid Resolution Issues for Vortical Flows on a Delta Wing and an F-18C," *AIAA 03-1103*, Jan 2003.
- [25] Parikh, P., Chung, J., "A Computational Study of the AWS Characteristics for Various Fighter Jets: Part I, F/A-18E & F-16C," *AIAA 03-0746*, Jan 2003.
- [26] Morton, S.A., Forsythe, J.R., Mitchell, A.M., and Hajek, D., "Detached-Eddy Simulations and Reynolds-Averaged Navier-Stokes Simulations of Delta Wing Vortical Flowfields," *Journal of Fluids Engineering*, **124**, No. 4, pp. 924-932, 2002.
- [27] Mitchell, A.M., Molton, P., Barberis, D., Dlery, J., "Oscillation of Vortex Breakdown Location and Control of the Time-Averaged Location by Blowing" *AIAA Journal*, **38**, No. 5, pp.793-803, May 2000.